INTERNATIONAL JOURNAL FOR NUMERICAL METHODS IN FLUIDS
Int. J. Numer. Meth. Fluids 2007; **53**:691–711
Published online 23 August 2006 in Wiley InterScience (www.interscience.wiley.com). DOI: 10.1002/fld.1300

Computational study of the axial instability of rimming flow using Arnoldi method

Sun Hyuk Bae[‡] and Do Hyun Kim[*, †]

Department of Chemical and Biomolecular Engineering & Center for Ultramicrochemical Process Systems, Korea Advanced Institute of Science and Technology, 373-1 Guseong-dong, Yuseong-gu, Daejeon 305-701, Korea

SUMMARY

Axial instability of rimming flow has been investigated by solving a linear generalized eigenvalue problem that governs the evolution of perturbations of two-dimensional base flow. Using the Galerkin finite element method, full Navier–Stokes equations were solved to calculate base flow and this base flow was perturbed with three-dimensional disturbances. The generalized eigenproblem formulated from these equations was solved by the implicitly restarted Arnoldi method using shift-invert technique. This study presents instability curves to identify the critical wavelength of the neutral mode and the critical β, which measures the importance of gravity relative to viscosity. The axial instability of rimming flow is examined and three-dimensional flow was reconstructed by using eigenvector and growth rate at a critical wave number. The critical β value in the axial instability analysis was observed to be comparable to the onset β value of the transition between the bump and the homogeneous film state in 2-D base flow calculations. Copyright © 2006 John Wiley & Sons, Ltd.

Received 14 April 2005; Revised 9 February 2006; Accepted 19 May 2006

KEY WORDS: rimming flow; axial instability; finite element method; Arnoldi method

1. INTRODUCTION

Coating flows are among an important class of flows commonly found in industrial applications. Rimming flow is the coating flow in a thin liquid layer on the inner surface of a horizontally rotating cylinder, which is of particular interest in rotational moulding from molten polymers, some pipe-coating processes and in the manufacture of pipes and columns from molten metals

[*]Correspondence to: Do Hyun Kim, Department of Chemical and Biomolecular Engineering & Center for Ultramicrochemical Process Systems, Korea Advanced Institute of Science and Technology, 373-1 Guseong-dong, Yuseong-gu, Daejeon 305-701, Korea.
[†]E-mail: DoHyun.Kim@kaist.ac.kr
[‡]E-mail: sunhyukbae@kaist.ac.kr

Contract/grant sponsor: BK 21
Contract/grant sponsor: KOSEF

and cements. Rimming flow problem provides basis to a number of different fluid mechanical problems involving free surface boundaries.

Much work related to rimming flow was initiated by Moffatt [1], who investigated the shape of the thin film that completely coats the outside of a horizontal rotating cylinder. Experimental and numerical work on the interface shape of a continuous film coating the interior of a rotating cylinder has described many interesting effects, including two-dimensional instabilities and time-periodic flows [2–7]. Two-dimensional (axially uniform) steady states are also observed experimentally, and analytical studies have been restricted to these References [1, 8–10]. Research in this area has overlapped work on coating the outside of a rotating cylinder, which is similar in certain regions of parameter space [11–16].

For rimming flows, most of previous analytical studies of two-dimensional steady-state solutions describing the interface height have focused on limits in which surface tension or inertia effect is negligible [3, 8–10, 17–26]. Since the complete lubrication equation for the interface height is a third-order non-linear differential equation in which the surface tension effects represent a singular perturbation, we expect that surface tension may have a significant effect on the qualitative and quantitative behaviours of the system, at least in some regions of parameter space. In addition, we expect that inertia effect is the one of the main factors inducing axial instability. In this paper, therefore, full Navier–Stokes equation including surface tension and inertia effect is used to investigate the various patterns of rimming flow.

While many researchers have conducted lubrication analysis and numerical simulation of rimming flow, axial instability analyses have not been extensively undertaken. Hosoi and Mahadevan [3] derived simplified model equations for the evolution of free surfaces using a small parameter α as a ratio of viscous to gravitational force. By applying small α approximation, they solved equations numerically using the finite difference method and then carried out linear instability analysis. For particle suspension in a partially filled horizontally rotating cylinder, which is a similar system to rimming flow, Govindarajan *et al.* [27, 28] analysed linear instability towards axial segregation and an undulation of the free surface at high particle concentrations over 10 wt%.

In this study, we first obtained 2-D base flow using the Galerkin finite element method. Then, we perturbed the base flow axially to investigate instability by solving a generalized eigenvalue problem [29–31]. As a result of this investigation, an onset condition for axial instability was discovered which is consistent with experimental results.

Among the methods employed to solve linear generalized eigenvalue problems, the Arnoldi method is likely the most popular. For many years, the Arnoldi method as a subspace iteration technique was considered less efficient than other methods because of the higher memory requirements. However, this difficulty has been overcome with the introduction of implicitly restarted iteration schemes. Moreover, the shift-invert technique can accelerate extraction of the eigenvalues and eigenvectors of interest. Thus, the implicitly restarted Arnoldi method with shift-invert technique is adopted in this study for the solution of the generalized eigenvalue problem.

In reporting the results of our 2-D base flow simulations, the deformation of the free surface shape occurs according to the change of the dimensionless numbers $\beta = F(gR/\Omega v)^{1/2}$, where F is the fluid filling fraction, g is the gravitational constant, R is the radius of the cylinder, Ω is the angular velocity of the rotating cylinder, $v = \mu/\rho$ is the kinematic viscosity of the liquid, ρ is the density, and μ is the viscosity. β measures the importance of gravitational force with respect to viscous force, taking the fluid filling fraction into account. β is the same parameter used in Tirumkudulu and Acrivos' work [21] and corresponds to $\Gamma^{1/2}$ in Johnson's work [8], $\omega^{-1/2}$ in Benjamin *et al.*'s work [20], and $\Lambda^{-1/2}$ in Melo's work [5]. Homogeneous film and bump states are

DOI: 10.1002/fld

characterized by the change of the average coating film thickness according to β. In our stability analysis, the effect of this parameter β on the instability of rimming flow was investigated.

2. GOVERNING EQUATIONS

For the calculation of 2-D steady base flow, the continuous liquid film inside a horizontal rotating cylinder is chosen as a numerical domain using a polar coordinate system with its origin at the axis of the cylinder. The equations for conservation of momentum and the continuity equation in dimensionless form with constant density and viscosity are

$$\begin{aligned} Re\,\boldsymbol{U}\cdot\nabla\boldsymbol{U} &= \nabla\cdot\boldsymbol{T} + St\,\boldsymbol{e}_y \\ \nabla\cdot\boldsymbol{U} &= 0 \end{aligned} \tag{1}$$

where $\boldsymbol{T} = -P\mathbf{I} + \nabla\boldsymbol{U} + \nabla\boldsymbol{U}^{\mathbf{T}}$ is a total stress tensor, $\boldsymbol{U}$ is a velocity vector, P is a pressure, $\mathbf{I}$ is an identity tensor, and $\boldsymbol{e}_y = (-\sin\theta\boldsymbol{e}_r - \cos\theta\boldsymbol{e}_\theta)$ is a unit vector in the direction of gravity. The Reynolds number $Re = \Omega R^2/\nu$ and the Stokes number $St = gR/\nu\Omega$ represent the relative magnitudes of inertia and gravity with respect to viscous force. Here the characteristic length, velocity and pressure are R, $R\Omega$ and $\mu\Omega$, respectively. Figure 1 shows the schematic geometry of rimming flow in a bump state. The unit vector normal to the surface $\boldsymbol{n}$ and unit tangential vector $\boldsymbol{t}$ are expressed in terms of interface height $H(\theta)$ as

$$\boldsymbol{n} = \frac{(-H, H_\theta)}{\sqrt{H^2 + H_\theta^2}} \quad \text{and} \quad \boldsymbol{t} = \frac{(H_\theta, H)}{\sqrt{H^2 + H_\theta^2}} \tag{2}$$

where H_θ is $\partial H/\partial\theta$.

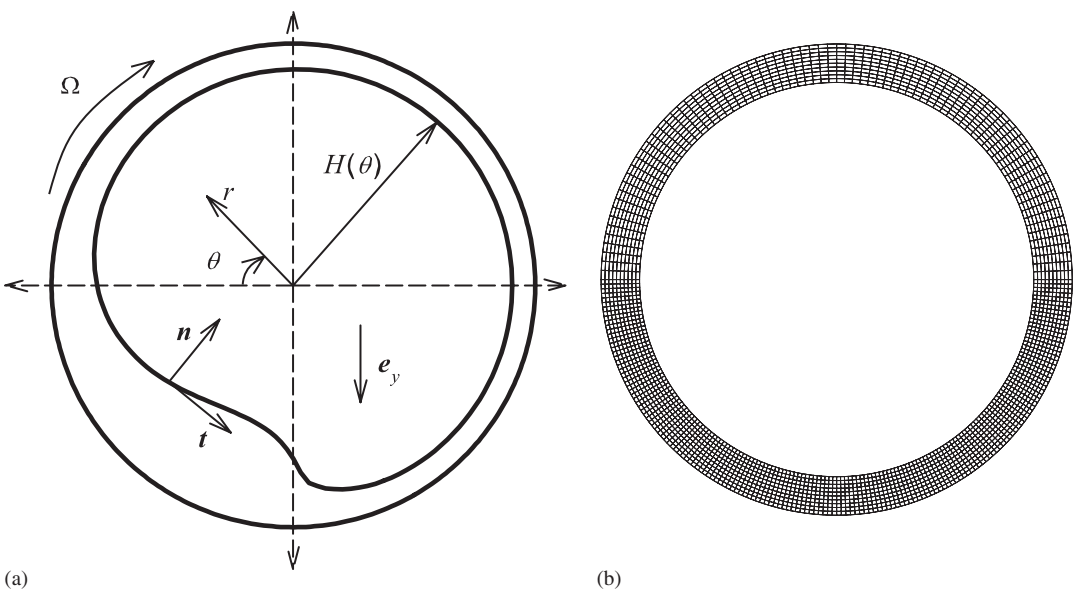

Figure 1. (a) 2-D cross-sectional schematic geometry of rimming flow with a bump; and (b) finite element mesh with 2400 elements.

DOI: 10.1002/fld

On the inner cylinder surface, the no-slip boundary condition yields $\boldsymbol{U} = (0, \Omega)$. On the gas/liquid meniscus, the kinematic condition and the tangential and normal stress balance conditions yield,

$$\begin{aligned} \boldsymbol{U} \cdot \boldsymbol{n} &= 0 \\ \boldsymbol{tn} : \boldsymbol{T} &= 0 \\ 2H &= Ca(\boldsymbol{nn} : \boldsymbol{T} - P_g) \end{aligned} \tag{3}$$

where $2H$ is a surface local mean curvature and P_g is a pressure difference across gas/liquid interface. According to the formulation used by Sackinger *et al.* [32], this pressure difference is calculated using the volume constraint for steady flows.

For the calculation of 3-D unsteady flow, the unsteady Navier–Stokes equation in polar coordinate system is expressed as

$$Re\left(\frac{\partial \boldsymbol{u}}{\partial t} + \boldsymbol{u} \cdot \nabla \boldsymbol{u}\right) = \nabla \cdot \boldsymbol{T} + St\, \boldsymbol{e}_y \tag{4}$$

where $\boldsymbol{u} = \boldsymbol{u}(r, \theta, z, t)$,

$$\nabla \boldsymbol{u} = \begin{bmatrix} \dfrac{\partial u}{\partial r} & \dfrac{\partial v}{\partial r} & \dfrac{\partial w}{\partial r} \\ \dfrac{1}{r}\left(\dfrac{\partial u}{\partial \theta} - v\right) & \dfrac{1}{r}\left(\dfrac{\partial v}{\partial \theta} + u\right) & \dfrac{1}{r}\dfrac{\partial w}{\partial \theta} \\ \dfrac{\partial u}{\partial z} & \dfrac{\partial v}{\partial z} & \dfrac{\partial w}{\partial z} \end{bmatrix}$$

$$\nabla \cdot \boldsymbol{T} = \begin{bmatrix} -P + 2\dfrac{\partial u}{\partial r} & \dfrac{\partial v}{\partial r} + \dfrac{1}{r}\left(\dfrac{\partial u}{\partial \theta} - v\right) & \dfrac{\partial w}{\partial r} + \dfrac{\partial u}{\partial z} \\ \dfrac{\partial v}{\partial r} + \dfrac{1}{r}\left(\dfrac{\partial u}{\partial \theta} - v\right) & -P + \dfrac{2}{r}\left(\dfrac{\partial v}{\partial \theta} + u\right) & \dfrac{1}{r}\dfrac{\partial w}{\partial \theta} + \dfrac{\partial v}{\partial z} \\ \dfrac{\partial w}{\partial r} + \dfrac{\partial u}{\partial z} & \dfrac{1}{r}\dfrac{\partial w}{\partial \theta} + \dfrac{\partial v}{\partial z} & -P + 2\dfrac{\partial w}{\partial z} \end{bmatrix}$$

with the result of 2-D steady flow as the initial condition and same boundary conditions as steady ones.

On the gas/liquid meniscus, the kinematic condition yields,

$$\frac{\partial h}{\partial t} + \boldsymbol{u} \cdot \boldsymbol{n} = 0 \tag{5}$$

3. NUMERICAL METHOD

The governing equations for the base flow are solved using the Galerkin finite element method for $\boldsymbol{U}$, P, H and P_g. The Newton–Raphson method is used to reformulate the discretized non-linear equations into linear equations that in turn are solved by the frontal solver [33]. Because

DOI: 10.1002/fld

the convergent solution of the Newton–Raphson method depends on an initial guess, all two-dimensional computations were conducted with the initial guess of uniform film thickness and then the β value was increased to produce the bump state. Based on these results, additional simulations were performed to investigate the effects of other parameters, such as viscosity, surface tension and cylinder radius.

For stability analysis, the base flow is perturbed using the disturbance velocity $\boldsymbol{u}'$, pressure p' and interfacial height h'. Then the total velocity, pressure and interfacial height can be written as

$$\begin{bmatrix} \boldsymbol{u}(r,\theta,z,t) \\ p(r,\theta,z,t) \\ h(\theta,z,t) \end{bmatrix} = \begin{bmatrix} \boldsymbol{U}(r,\theta) \\ P(r,\theta) \\ H(\theta) \end{bmatrix} + \begin{bmatrix} \boldsymbol{u}'(r,\theta,z,t) \\ p'(r,\theta,z,t) \\ h'(\theta,z,t) \end{bmatrix} \tag{6}$$

Using these variables, the equation of motion and the continuity equation are weak formulated for the finite element method as

r-directional component:

$$\int_D \left(\begin{array}{l} \Phi_i^V \mathrm{e}^{-\mathrm{j}mz} Re \left(\dfrac{\partial u}{\partial t} + u\dfrac{\partial u}{\partial r} + \dfrac{v}{r}\dfrac{\partial u}{\partial \theta} - \dfrac{v^2}{r} + w\dfrac{\partial u}{\partial z} + St\sin\theta \right) \\ \quad + \dfrac{\partial \Phi_i^V}{\partial r}\mathrm{e}^{-\mathrm{j}mz}\left(-P + 2\dfrac{\partial u}{\partial r}\right) + \dfrac{1}{r}\dfrac{\partial \Phi_i^V}{\partial \theta}\mathrm{e}^{-\mathrm{j}mz}\left(\dfrac{\partial v}{\partial r} - \dfrac{v}{r} + \dfrac{1}{r}\dfrac{\partial u}{\partial \theta}\right) \\ \quad + \dfrac{\Phi_i^V}{r}\mathrm{e}^{-\mathrm{j}mz}\left(-P + \dfrac{2}{r}\left(\dfrac{\partial v}{\partial \theta} + u\right)\right) + \dfrac{\partial(\Phi_i^V \mathrm{e}^{-\mathrm{j}mz})}{\partial z}\left(\dfrac{\partial w}{\partial r} + \dfrac{\partial u}{\partial z}\right) \end{array} \right) \mathrm{d}D = 0 \tag{7}$$

θ-directional component:

$$\int_D \left(\begin{array}{l} \Phi_i^V \mathrm{e}^{-\mathrm{j}mz} Re \left(\dfrac{\partial v}{\partial t} + u\dfrac{\partial v}{\partial r} + \dfrac{v}{r}\dfrac{\partial v}{\partial \theta} + \dfrac{uv}{r} + w\dfrac{\partial v}{\partial z} + St\cos\theta \right) \\ \quad + \left(\dfrac{\partial \Phi_i^V}{\partial r}\mathrm{e}^{-\mathrm{j}mz} - \dfrac{\Phi_i^V \mathrm{e}^{-\mathrm{j}mz}}{r} \right)\left(\dfrac{\partial v}{\partial r} - \dfrac{v}{r} + \dfrac{1}{r}\dfrac{\partial u}{\partial \theta}\right) \\ \quad + \dfrac{1}{r}\dfrac{\partial \Phi_i^V}{\partial \theta}\mathrm{e}^{-\mathrm{j}mz}\left(-P + \dfrac{2}{r}\left(\dfrac{\partial v}{\partial \theta} + u\right)\right) + \dfrac{\partial(\Phi_i^V \mathrm{e}^{-\mathrm{j}mz})}{\partial z}\left(\dfrac{1}{r}\dfrac{\partial w}{\partial \theta} + \dfrac{\partial v}{\partial z}\right) \end{array} \right) \mathrm{d}D = 0 \tag{8}$$

z-directional component:

$$\int_D \left(\begin{array}{l} \Phi_i^V \mathrm{e}^{-\mathrm{j}mz} Re \left(\dfrac{\partial w}{\partial t} + u\dfrac{\partial w}{\partial r} + \dfrac{v}{r}\dfrac{\partial w}{\partial \theta} + w\dfrac{\partial w}{\partial z} \right) \\ \quad + \dfrac{\partial \Phi_i^V}{\partial r}\mathrm{e}^{-\mathrm{j}mz}\left(\dfrac{\partial w}{\partial r} + \dfrac{\partial u}{\partial z}\right) + \dfrac{1}{r}\dfrac{\partial \Phi_i^V}{\partial \theta}\mathrm{e}^{-\mathrm{j}mz}\left(\dfrac{1}{r}\dfrac{\partial w}{\partial \theta} + \dfrac{\partial v}{\partial z}\right) \\ \quad + \dfrac{\partial(\Phi_i^V \mathrm{e}^{-\mathrm{j}mz})}{\partial z}\left(-P + 2\dfrac{\partial w}{\partial z}\right) \end{array} \right) \mathrm{d}D = 0 \tag{9}$$

DOI: 10.1002/fld

and the continuity equation:

$$\int_D \Phi_i^P \mathrm{e}^{-\mathrm{j}mz}\left(\frac{\partial u}{\partial r}+\frac{u}{r}+\frac{1}{r}\frac{\partial v}{\partial \theta}+\frac{\partial w}{\partial z}\right)\mathrm{d}D=0 \tag{10}$$

where D is the numerical domain, Φ_i^V is the biquadratic basis function for velocity and Φ_i^P is the piecewise linear basis function for pressure. For simplified treatment of the complex equations, $\mathrm{e}^{-\mathrm{j}mz}$ is multiplied by the basis function Φ and used as a weight function.

In terms of normal mode, we represent the disturbances of the velocities, pressure and interfacial height in a symmetry plane as

$$\begin{bmatrix} \boldsymbol{u}(r,\theta,z,t) \\ p(r,\theta,z,t) \\ h(\theta,z,t) \end{bmatrix} = \begin{bmatrix} \boldsymbol{U}(r,\theta) \\ P(r,\theta) \\ H(\theta) \end{bmatrix} + \sum_{m=-\infty}^{\infty} \begin{bmatrix} \mathrm{j}\tilde{u}_m(r,\theta) \\ \mathrm{j}\tilde{v}_m(r,\theta) \\ \tilde{w}_m(r,\theta) \\ \mathrm{j}\tilde{p}_m(r,\theta) \\ \mathrm{j}\tilde{h}_m(\theta) \end{bmatrix} \exp(\sigma_m t+\mathrm{j}mz) \tag{11}$$

where $\mathrm{j}=\sqrt{-1}$ is the imaginary unit, m is a spanwise wave number and $\sigma_m=\sigma_{r,m}+\mathrm{j}\sigma_{i,m}$ is the complex growth rate. The reason for the choice of the imaginary amplitude in normal modes except for the axial velocity w is to avoid the complex arithmetic in the subsequent calculation of the eigenproblem [34]. The assumed form of the eigenvector is completely general and allows for both steady and oscillatory modes, depending on whether the eigenvalue σ_m is real or complex, respectively. This normal mode form also includes the time-dependent two-dimensional instability of the steady flow for which $m=0$. Substituting these normal modes into the equations of motion and the continuity equation yields an eigenvalue problem with the growth rate being the eigenvalue ($\mathrm{e}^{\sigma t+\mathrm{j}mz}$, $\mathrm{e}^{-\mathrm{j}mz}$ and subscript m are removed for simplification).

r-directional component:

$$\sum_{D_e=1}^{\mathrm{NE}} \int_{-1}^{1}\int_{-1}^{1} \left[\begin{array}{l} (\tilde{r}\bar{\mathrm{J}}+\bar{r}\tilde{\mathrm{J}})\left[\Phi_i^V\left(Re\left(\bar{r}U\dfrac{\partial U}{\partial \bar{r}}+V\dfrac{\partial U}{\partial \theta}-\bar{\mathrm{J}}V^2\right)+\bar{r}\bar{\mathrm{J}}\,St\sin\theta\right)\right] \\ \quad +\bar{r}\bar{\mathrm{J}}\left[\Phi_i^V Re\left(\begin{array}{l}\bar{r}\bar{\mathrm{J}}\left(\sigma\tilde{u}-\dfrac{\partial U}{\partial \bar{r}}\dfrac{\Delta\bar{r}}{\Delta H}\sigma\tilde{h}\right)+\tilde{r}U\dfrac{\partial U}{\partial \bar{r}}+\bar{r}U\dfrac{\partial \tilde{u}}{\partial \bar{r}} \\ \quad +\tilde{v}\dfrac{\partial U}{\partial \theta}+V\dfrac{\partial \tilde{u}}{\partial \theta}+V\dfrac{\partial U}{\partial \tilde{\theta}}-\tilde{\mathrm{J}}V^2-2\bar{\mathrm{J}}V\tilde{v}\end{array}\right)+\Phi_i^V(\tilde{r}\bar{\mathrm{J}}+\bar{r}\tilde{\mathrm{J}})\,St\sin\theta\right] \\ \quad +\left(\begin{array}{l}\tilde{r}\dfrac{\partial\Phi_i^V}{\partial\bar{r}}\left(-\bar{r}\bar{\mathrm{J}}\bar{P}+2\bar{r}\dfrac{\partial U}{\partial\bar{r}}\right)+\bar{r}\dfrac{\partial\Phi_i^V}{\partial\bar{r}}\left(-(\tilde{r}\bar{\mathrm{J}}+\bar{r}\tilde{\mathrm{J}})\bar{P}-\bar{r}\bar{\mathrm{J}}\tilde{P}+2\tilde{r}\dfrac{\partial U}{\partial\bar{r}}+2\bar{r}\dfrac{\partial\tilde{u}}{\partial\bar{r}}\right) \\ \quad +\dfrac{\partial\Phi_i^V}{\partial\tilde{\theta}}\left(\bar{r}\dfrac{\partial V}{\partial\bar{r}}-\bar{\mathrm{J}}V+\dfrac{\partial U}{\partial\theta}\right)+\dfrac{\partial\Phi_i^V}{\partial\theta}\left(\tilde{r}\dfrac{\partial V}{\partial\bar{r}}+\bar{r}\dfrac{\partial\tilde{v}}{\partial\bar{r}}-\tilde{\mathrm{J}}V-\bar{\mathrm{J}}\tilde{v}+\dfrac{\partial U}{\partial\tilde{\theta}}+\dfrac{\partial\tilde{u}}{\partial\theta}\right) \\ \quad +\tilde{\mathrm{J}}\Phi_i^V\left(-\bar{r}\bar{\mathrm{J}}\bar{P}+2\left(\dfrac{\partial V}{\partial\theta}+\bar{\mathrm{J}}U\right)\right)+\bar{r}\bar{\mathrm{J}}(-m\Phi_i^V)\left(\bar{r}\dfrac{\partial\tilde{w}}{\partial\bar{r}}+\bar{r}\bar{\mathrm{J}}(-m\tilde{u})\right) \\ \quad +\bar{\mathrm{J}}\Phi_i^V\left(-(\tilde{r}\bar{\mathrm{J}}+\bar{r}\tilde{\mathrm{J}})\bar{P}-\bar{r}\bar{\mathrm{J}}\tilde{P}+2\left(\dfrac{\partial V}{\partial\tilde{\theta}}+\dfrac{\partial\tilde{v}}{\partial\theta}+\tilde{\mathrm{J}}U+\bar{\mathrm{J}}u\right)\right)\end{array}\right)\end{array}\right]\mathrm{d}\xi\,\mathrm{d}\eta=0 \tag{12}$$

DOI: 10.1002/fld

θ-directional component:

$$\sum_{D_e=1}^{\mathrm{NE}} \int_{-1}^{1}\int_{-1}^{1} \left[\begin{array}{l} ((\tilde{r}\bar{\mathrm{J}}+\bar{r}\tilde{\mathrm{J}})(H^2+H_\theta^2)+\bar{r}\bar{\mathrm{J}}2(H\tilde{h}+H_\theta\tilde{h}_\theta)) \left[\Phi_i^V \left(\begin{array}{l} Re\left(\bar{r}U\dfrac{\partial V}{\partial \bar{r}}+V\dfrac{\partial V}{\partial \theta}+\bar{\mathrm{J}}UV\right) \\ \quad +\bar{r}\bar{\mathrm{J}}\,St\cos\theta \end{array} \right) \right] \\ \quad +\bar{r}\bar{\mathrm{J}}(H^2+H_\theta^2) \left[\begin{array}{l} \Phi_i^V\, Re \left(\begin{array}{l} \bar{r}\bar{\mathrm{J}}\left(\sigma\tilde{v}-\dfrac{\partial V}{\partial \bar{r}}\dfrac{\Delta\bar{r}}{\Delta H}\sigma\tilde{h}\right)+\tilde{r}U\dfrac{\partial V}{\partial \bar{r}}+\bar{r}\tilde{u}\dfrac{\partial V}{\partial \bar{r}}+\bar{r}U\dfrac{\partial \tilde{v}}{\partial \bar{r}}+\tilde{v}\dfrac{\partial V}{\partial \theta} \\ \quad +V\dfrac{\partial V}{\partial \tilde{\theta}}+V\dfrac{\partial v}{\partial \theta}+\tilde{\mathrm{J}}UV+\bar{\mathrm{J}}\tilde{u}V+\bar{\mathrm{J}}U\tilde{v} \end{array} \right) \\ \quad +\Phi_i^V(\tilde{r}\bar{\mathrm{J}}+\bar{r}\tilde{\mathrm{J}})\,St\cos\theta \end{array} \right] \\ \quad +2(H\tilde{h}+H_\theta\tilde{h}_\theta) \left[\begin{array}{l} \left(\bar{r}\dfrac{\partial\Phi_i^V}{\partial\bar{r}}-\bar{\mathrm{J}}\Phi_i^V\right)\left(\bar{r}\dfrac{\partial V}{\partial\bar{r}}-\bar{\mathrm{J}}V+\dfrac{\partial U}{\partial\theta}\right) \\ \quad +\dfrac{\partial\Phi_i^V}{\partial\theta}\left(-\bar{r}\bar{\mathrm{J}}\bar{P}+2\left(\dfrac{\partial V}{\partial\theta}+\bar{\mathrm{J}}U\right)\right) \end{array} \right] \\ \quad +(H^2+H_\theta^2) \left[\begin{array}{l} \left(\tilde{r}\dfrac{\partial\Phi_i^V}{\partial\bar{r}}-\tilde{\mathrm{J}}\Phi_i^V\right)\left(\bar{r}\dfrac{\partial V}{\partial\bar{r}}-\bar{\mathrm{J}}V+\dfrac{\partial U}{\partial\theta}\right) \\ \quad +\left(\bar{r}\dfrac{\partial\Phi_i^V}{\partial\bar{r}}-\bar{\mathrm{J}}\Phi_i^V\right)\left(\tilde{r}\dfrac{\partial V}{\partial\bar{r}}+\bar{r}\dfrac{\partial\tilde{v}}{\partial\bar{r}}-\tilde{\mathrm{J}}V-\bar{\mathrm{J}}\tilde{v}+\dfrac{\partial U}{\partial\tilde{\theta}}+\dfrac{\partial\tilde{u}}{\partial\theta}\right) \\ \quad +\dfrac{\partial\Phi_i^V}{\partial\tilde{\theta}}\left(-\bar{r}\bar{\mathrm{J}}\bar{P}+2\left(\dfrac{\partial V}{\partial\theta}+\bar{\mathrm{J}}U\right)\right) \\ \quad +\dfrac{\partial\Phi_i^V}{\partial\theta}\left(-(\tilde{r}\bar{\mathrm{J}}+\bar{r}\tilde{\mathrm{J}})\bar{P}-\bar{r}\bar{\mathrm{J}}\tilde{P}+2\left(\dfrac{\partial V}{\partial\tilde{\theta}}+\dfrac{\partial\tilde{v}}{\partial\theta}+\tilde{\mathrm{J}}U+\bar{\mathrm{J}}\tilde{u}\right)\right) \\ \quad +\bar{r}\bar{\mathrm{J}}(-m\Phi_i^V)\left(\bar{r}\bar{\mathrm{J}}(-m\tilde{v})+\dfrac{\partial\tilde{w}}{\partial\theta}\right) \end{array} \right] \end{array} \right] \mathrm{d}\xi\,\mathrm{d}\eta=0 \tag{13}$$

z-directional component:

$$\sum_{D_e=1}^{\mathrm{NE}} \int_{-1}^{1}\int_{-1}^{1} \left[\begin{array}{l} \bar{r}\bar{\mathrm{J}}\Phi_i^V Re\left(\bar{r}\bar{\mathrm{J}}(\sigma\tilde{w})+\bar{r}U\dfrac{\partial\tilde{w}}{\partial\bar{r}}+V\dfrac{\partial\tilde{w}}{\partial\theta}\right) \\ \quad +\bar{r}\dfrac{\partial\Phi_i^V}{\partial\bar{r}}\left(\bar{r}\dfrac{\partial\tilde{w}}{\partial\bar{r}}+\bar{r}\bar{\mathrm{J}}(-m\tilde{u})\right)+\dfrac{\partial\Phi_i^V}{\partial\theta}\left(\bar{r}\bar{\mathrm{J}}(-m\tilde{v})+\dfrac{\partial\tilde{w}}{\partial\theta}\right) \\ \quad +m\Phi_i^V\bar{r}\bar{\mathrm{J}}(-2\bar{P}(\tilde{r}\bar{\mathrm{J}}+\bar{r}\tilde{\mathrm{J}})-\bar{r}\bar{\mathrm{J}}\bar{P}+2\bar{r}\bar{\mathrm{J}}(m\tilde{w})) \end{array} \right] \mathrm{d}\xi\,\mathrm{d}\eta=0 \tag{14}$$

continuity equation:

$$\sum_{D_e=1}^{\mathrm{NE}} \int_{-1}^{1}\int_{-1}^{1} \left[\Phi_i^P \left(\tilde{r}\frac{\partial U}{\partial\bar{r}}+\bar{r}\frac{\partial\tilde{u}}{\partial\bar{r}}+\tilde{\mathrm{J}}U+\bar{\mathrm{J}}\tilde{u}+\frac{\partial V}{\partial\tilde{\theta}}+\frac{\partial\tilde{v}}{\partial\theta}+\bar{r}\bar{\mathrm{J}}(m\tilde{w}) \right) \right] \mathrm{d}\xi\,\mathrm{d}\eta=0 \tag{15}$$

DOI: 10.1002/fld

where NE is the total number of elements. Finally, the kinematic condition on the interface, Equation (5), is modified and used as the equation to solve $\tilde{h}$ as

$$-H\sigma\tilde{h} + (-\tilde{h}U + H\tilde{u}) + \left(\frac{\partial\tilde{h}}{\partial\theta}V + H_\theta\tilde{v}\right) = 0 \tag{16}$$

For the calculation of the free surface deformation, we employed the spine method developed by Saito and Scriven [35], wherein mesh nodes that are free to move lie on generator lines called spines. The position of a node is represented parametrically as

$$\begin{aligned} r_i &= \alpha_r(h_{j+1} + \zeta_i(h_j - h_{j+1})) + \psi_r \\ \theta_i &= \alpha_\theta(h_{j+1} + \zeta_i(h_j - h_{j+1})) + \psi_\theta \\ z_i &= \alpha_z(h_{j+1} + \zeta_i(h_j - h_{j+1})) + \psi_z \end{aligned} \tag{17}$$

where h_j is the interface local parameter for a given spine, $\alpha = (-1, 0, 0)$ is the direction vector, and $\psi = (R, 0, 0)$ is the base point of the spine. In this study ψ is on the cylinder. The location (r_i, θ_i, z_i) of a node on the spine which is free to move is determined from its relative position, ζ_i, to the moving interfaces located at h_j and h_{j+1}. This parametric approach allows the initial aspect ratio of the nodes on a spine to be easily maintained as each node on a spine will retain the same relative position between the interfaces. Also note that each of the spines is independent of the other spines. The interface location parameters, h_j, are the new degrees of freedom introduced.

$\partial/\partial t$ is the Eulerian time derivative; that is, the nodal velocity field must be for nodes fixed in space. However, the technique of parameterization of the free surface is such that the nodes are not fixed in some frame of reference as in the Eulerian formulation, nor are they fixed in a frame of reference carried along by the fluid as in the Lagrangian formulation; rather each node is constrained to move along a fixed line (spine) in space—a mixed Eulerian–Lagrangian formulation. Thus, the Eulerian time derivatives in Navier–Stokes equations must be transformed to time derivatives $\delta/\delta t$ which follow the moving nodes along these lines. Since any given node will always transform to the same fixed point in the local space, this derivative can be thought of as a time derivative at a fixed point in the local coordinate frame.

$$\frac{\delta u}{\delta t} = \frac{\partial u}{\partial t} + \frac{\delta h}{\delta t}\frac{\Delta r}{\Delta h}\frac{\partial u}{\partial r} \tag{18}$$

Three components appear in the denominators of the weak formulations which are: (i) J, the determinant of the Jacobian matrix of global coordinates with respect to local coordinates same, (ii) r, the distance from the axis of the cylinder to the node of the on-going global element, and (iii) $(h^2 + h_\theta^2)$ which is derived from the free surface boundary condition treatment. Therefore, we multiplied the r-, θ- and z-directional components of the momentum equation by $r\mathrm{J}, r\mathrm{J}(h^2 + h_\theta^2)$ and $r\mathrm{J}$, respectively, in order to simplify the weak formulated equations. r and J are variables dependent on the interfacial height, so the derivations of two variables are represented by the derivation of the interfacial height according to the following

DOI: 10.1002/fld

relation:

$$
\begin{aligned}
r &= \bar{r} + \tilde{r} = \bar{r} + \frac{\partial \bar{r}}{\partial h} = \bar{r} + \alpha_r \sum_l \omega_l \frac{\partial}{\partial r_l} \left(\sum_k r_k \Phi_k \right) = \alpha_r \sum_l \omega_l \Phi_l \\
J &= \bar{\mathrm{J}} + \tilde{\mathrm{J}} = \bar{\mathrm{J}} + \frac{\partial \bar{\mathrm{J}}}{\partial h} = \bar{\mathrm{J}} + \alpha_r \sum_l \omega_l \frac{\partial}{\partial r_l} \left[\frac{\partial}{\partial \xi} \left(\sum_k r_k \Phi_k \right) \frac{\partial \theta}{\partial \eta} - \frac{\partial \theta}{\partial \xi} \frac{\partial}{\partial \eta} \left(\sum_k r_k \Phi_k \right) \right] \\
&= \bar{\mathrm{J}} + \alpha_r \sum_l \omega_l \left[\frac{\partial \Phi_l}{\partial \xi} \frac{\partial \theta}{\partial \eta} - \frac{\partial \theta}{\partial \xi} \frac{\partial \Phi_l}{\partial \eta} \right]
\end{aligned}
\tag{19}
$$

where $\bar{r}$ and $\bar{\mathrm{J}}$ are the steady-state values, $\tilde{r}$ and $\tilde{\mathrm{J}}$ are the perturbed values represented by perturbed interfacial height, $\alpha_r = 1$ is the r-directional component of a direction vector for a given spine and ω_l is the relative position of the nodes from the outer cylinder to the moving interface.

The discrete form of Equations (12)–(15) is obtained by evaluating the integrals using a nine-point Gaussian quadrature. Let $\boldsymbol{Y}$ denote an unknown vector, with dimension L, consisting of the perturbation velocity, pressure and interfacial height to be determined. Then Equations (12)–(15) can be written as the generalized matrix eigenvalue problem

$$
\boldsymbol{A}\boldsymbol{Y} = \sigma \boldsymbol{B}\boldsymbol{Y} \tag{20}
$$

where $\boldsymbol{A} \in \boldsymbol{R}^{L \times L}$ is a non-symmetric matrix, and $\boldsymbol{B} \in \boldsymbol{R}^{L \times L}$ is a real-valued, symmetric matrix. The matrix $\boldsymbol{B}$ is singular with N rows (the number of the pressure variables) in it being identically zero (due to the absence of a time-derivative in the continuity equation). In addition, the homogeneous essential boundary conditions on the discrete perturbation vector $\boldsymbol{Y}$ are directly imposed in the discrete form of Equation (20), by setting all the entries in the corresponding row of the matrices $\boldsymbol{A}$ and $\boldsymbol{B}$ to zero, except for the diagonal entry in $\boldsymbol{A}$ which is set to unity (this is seen to have the desired effect of forcing the corresponding nodal value in $\boldsymbol{Y}$ to zero).

The linearized instability of the base flow at different β can be determined from the eigenvalues of σ of Equation (20). For sufficiently large β, all eigenvalues have $Re(\sigma) < 0$ so that the corresponding eigenmodes will decay. There is a critical value β_c at which the leading eigenvalue (i.e. the eigenvalue with the maximum real part) crosses the imaginary axis into the right half-plane so that the corresponding eigenmode is linearly unstable. If the corresponding imaginary part of this leading eigenvalue is zero at β_c, then we have a regular bifurcation to a steady secondary solution. However, if it is non-zero, so that crossing occurs for a complex-conjugate pair of eigenvalues, then we have a Hopf bifurcation to a time-periodic secondary solution, whose frequency at the onset of this instability is determined by the magnitude of the imaginary part of the eigenvalue at this crossing [34].

If the eigenspectrum shows Hopf mode behaviour, the reconstructed velocity and interfacial height are [34]:

$$
\begin{aligned}
u &= U - 2\,\mathrm{e}^{\sigma_r t}[\tilde{u}_i \cos(\sigma_i t) + \tilde{u}_r \sin(\sigma_i t)][\cos(mz) + \mathrm{j} \sin(mz)] \\
v &= V - 2\,\mathrm{e}^{\sigma_r t}[\tilde{v}_i \cos(\sigma_i t) + \tilde{v}_r \sin(\sigma_i t)][\cos(mz) + \mathrm{j} \sin(mz)] \\
w &= 2\,\mathrm{e}^{\sigma_r t}[\tilde{w}_r \cos(\sigma_i t) - \tilde{w}_i \sin(\sigma_i t)][\cos(mz) + \mathrm{j} \sin(mz)] \\
h &= H - 2\,\mathrm{e}^{\sigma_r t}[\tilde{h}_i \cos(\sigma_i t) + \tilde{h}_r \sin(\sigma_i t)][\cos(mz) + \mathrm{j} \sin(mz)]
\end{aligned}
\tag{21}
$$

DOI: 10.1002/fld

where the subscript 'r' denotes the real part of an eigenvalue or eigenvector and the subscript 'i' denotes the imaginary part. If the eigenspectrum does not show Hopf mode behaviour, the reconstructed variables are

$$\begin{aligned} u &= U + \tilde{u}_r \, \mathrm{e}^{\sigma_r t}[-\sin(mz) + \mathrm{j}\cos(mz)] \\ v &= V + \tilde{v}_r \, \mathrm{e}^{\sigma_r t}[-\sin(mz) + \mathrm{j}\cos(mz)] \\ w &= \tilde{w}_r \, \mathrm{e}^{\sigma_r t}[\cos(mz) + \mathrm{j}\sin(mz)] \\ h &= H + \tilde{h}_r \, \mathrm{e}^{\sigma_r t}[-\sin(mz) + \mathrm{j}\cos(mz)] \end{aligned} \tag{22}$$

The matrices $\boldsymbol{A}$ and $\boldsymbol{B}$ are banded for an appropriate ordering of the nodes and unknowns in the computational mesh. Furthermore, in the present application, only the eigenvalues of Equation (20) in the least stable region of the spectrum are of interest. A suitable numerical scheme is described in Natarajan's work [36], which exploits the specific characteristics of these stability applications to efficiently perform relevant eigenvalue computations. That is, a shift-invert transformation with a designated complex shift λ is used to transform Equation (20) to,

$$\boldsymbol{KY} = (\boldsymbol{A} - \lambda \boldsymbol{B})^{-1} \boldsymbol{BY} = \hat{\sigma} \boldsymbol{Y}, \quad \hat{\sigma} = \frac{1}{\sigma - \lambda} \tag{23}$$

which is a standard eigenvalue problem for the complex, non-symmetric matrix $\boldsymbol{K}$. A restarted, iterative Arnoldi algorithm [37] is then used to solve Equation (23). The computationally expensive part of this algorithm is the matrix–vector products involving $\boldsymbol{K}$, which can be efficiently carried out without explicitly forming $\boldsymbol{K}$, by first performing the matrix–vector product with $\boldsymbol{B}$, followed by forward and backward substitution with the band diagonal factors of $\boldsymbol{A} - \lambda \boldsymbol{B}$. Because the eigenvalue near the zero imaginary axis is important to decide stability, we used the shift value as zero for all the computation.

The details of the algorithm of the Arnoldi method for a generalized eigenvalue problem have been reported elsewhere [37–39] and we use the implicitly restarted Arnoldi method with shift-invert technique available in the form of a public library ARPACK [40].

Figure 1(b) depicts the finite element mesh for the computational domain. After the convergence test for the grid size, we found that 2400-element grid as many as 10 080 nodes which was dense at the bottom of the cylinder is adequate for obtaining grid-invariant results for the bump states; however, the coarser mesh with 400 elements is sufficient for the homogeneous film state.

4. RESULTS AND DISCUSSION

4.1. Two-dimensional base flow

As has been firmly established, the structure of the flow depends on the values of four independent parameters: (a) the Reynolds number Re; (b) the filling fraction F; (c) the Stokes number St; and (d) the capillary number Ca. By fixing the value of surface tension, we are then left with three independent parameters of which F and St can be combined into the single parameter $\beta = F\,St^{1/2}$. We have observed that the shape of rimming flow and the aspect of the flow dynamics vary according to Re and β. Figure 2 depicts the variation of the meniscus shape according to Re and β. The coating film with originally uniform thickness deforms to have a bump and the flow inside the bump begins to recirculate as β increases over 1.59. In order to specify the critical β at which

DOI: 10.1002/fld

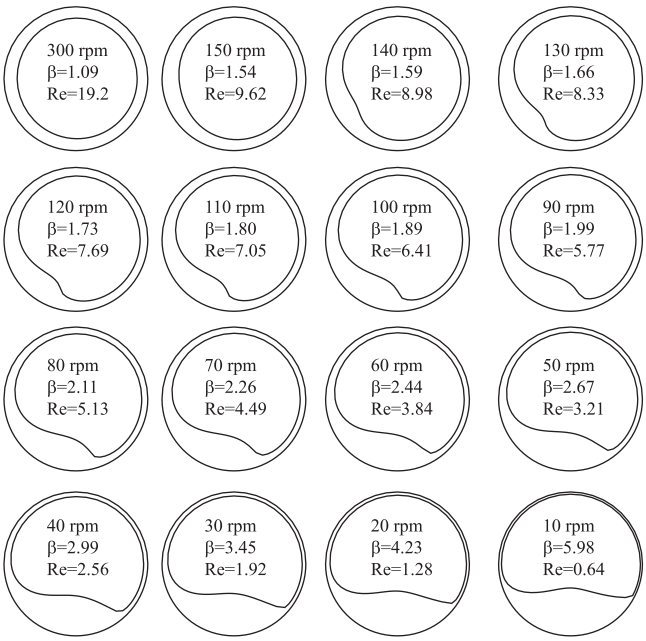

Figure 2. Change of free surface shape according to rotation speed. $F = 0.3$, $v = 500cSt$, $R = 1.75$ cm.

the rimming flow shape deforms, we investigated the variation of the average thickness of the coating film in relation to the variation of the controllable parameters and found that, as shown in Figure 3, the critical β is in the range of 1.4–1.6. (In previous papers using the thin lubrication approximation [3, 8, 20, 21], lubrication analysis leads to a discontinuous film profile for β larger than about 1.4.)

Using the results of two-dimensional flow simulations, we perturbed the velocity, pressure and interfacial height along axial direction and investigated the instability.

4.2. Convergence test

The convergence of the Arnoldi method was tested as shown in Figure 4. First, the results of three different mesh sizes ($M1 = 2000$, $M2 = 2400$ and $M3 = 4160$ elements) are shown in Figure 4(a) at $F = 0.1$, $\beta = 3.90$, $m = 1$. NEV (the number of eigenvalues of interest) and NCV (the number of Krylov subspace sets) are 30 and 100, respectively. The convergence test demonstrates good agreements among three different mesh sizes. A 2400-element mesh was then employed for the rest of computations. Figure 4(b) depicts the results of the convergence test according to the variation of NEV and NCV under the same computational conditions as in Figure 4(a). Essentially identical eigenspectra were obtained as NEV and NCV varied.

For the remainder of the computation, 30 eigenvalues were obtained, with an initial Krylov basis set of dimension 100 and a tolerance of 10^{-12} in the Arnoldi iterations. The accuracy of the converged eigenpairs was independently checked by evaluating the residual $\max_i |(\boldsymbol{A}_{ij} - \sigma \boldsymbol{B}_{ij})\boldsymbol{Y}_{ij}|$. This quantity was consistently less than 10^{-9} for the reported results. More importantly, for a few leading eigenpairs, this residual was less than 10^{-12}.

DOI: 10.1002/fld

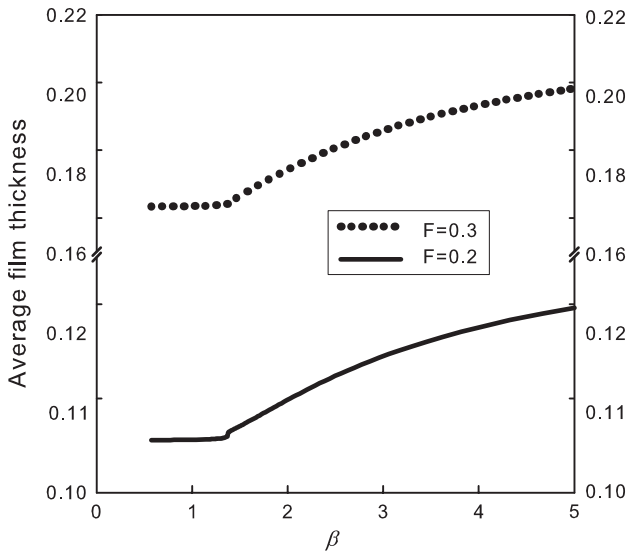

Figure 3. The change of the average thickness of the coating film inside the cylinder according to the dimensionless parameter β at $F = 0.2$ and 0.3.

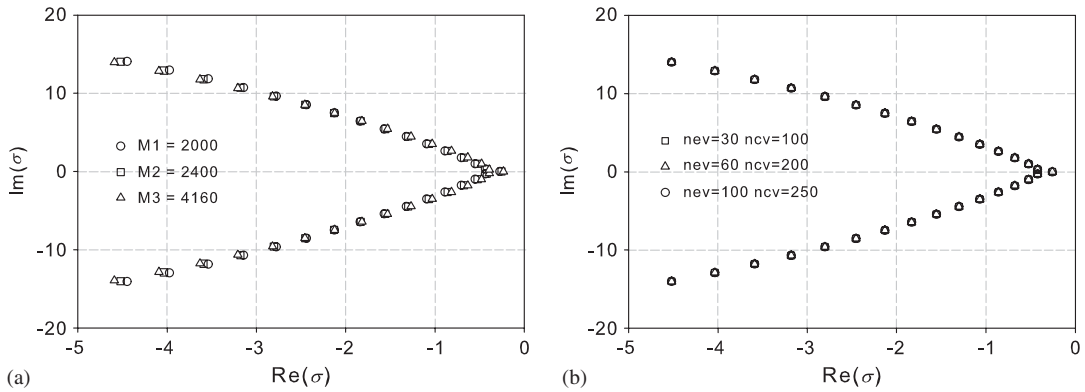

Figure 4. (a) Mesh refinement test ($M1 = 2000$, $M2 = 2400$, $M3 = 4160$) at $F = 0.1$, $\beta = 3.90$, $m = 1$, 30 eigenvalues and 100 Krylov subspaces; and (b) eigenvalue distribution for three subspace sets with $m = 1$, $M2$.

4.3. Reconstructed flow field

For comparison of our numerical results to experimental ones, we conducted rimming flow experiments with the apparatus similar to the previous work [21]. The radius of the Plexiglas cylinder is 3.5 cm and the axial length is 35 cm. Both end caps are also transparent and facilitates the cross-sectional view. Silicone oil (dimethylpolysiloxane) with various viscosity (100–5000*cSt*) and a mixture of glycerin and water are used as working fluid. The surface tension of silicone oil and the mixture of glycerin and water are 21 and 65 dyn/cm at 25°C, respectively.

DOI: 10.1002/fld

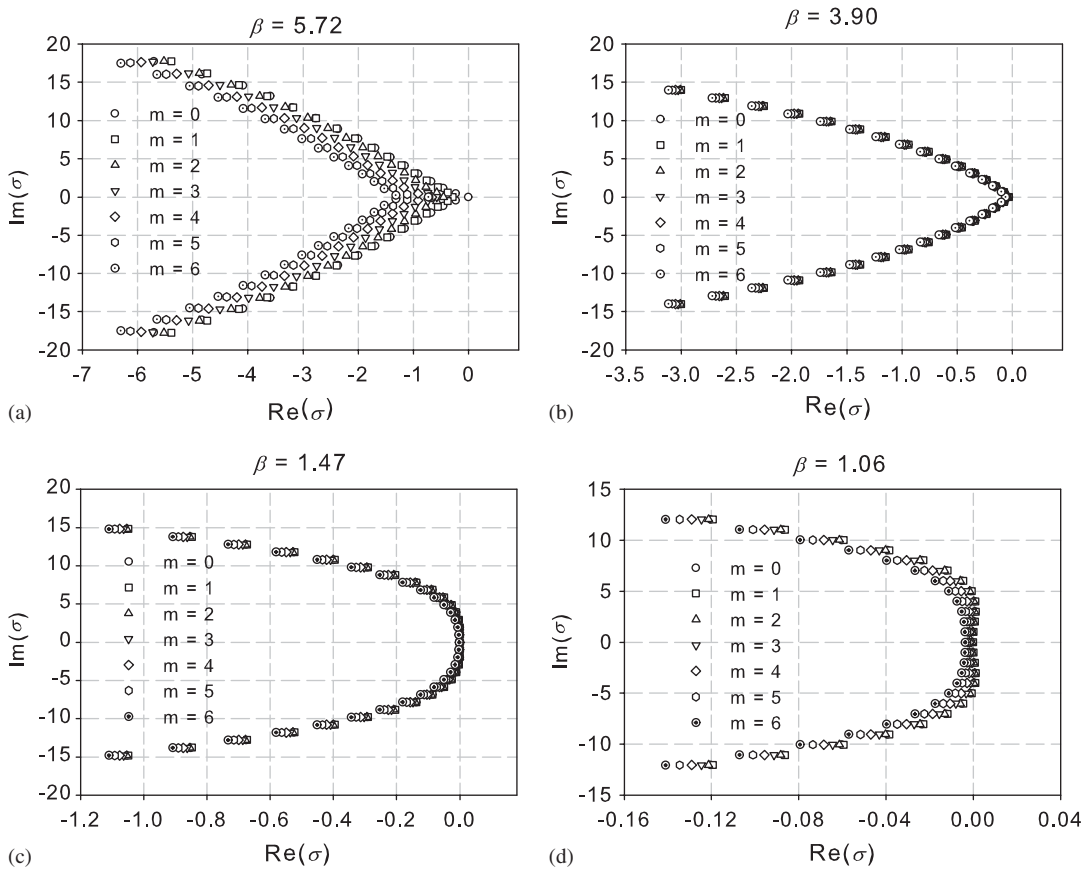

Figure 5. Variation of eigenspectrum as β decreases. At $\beta = 1.47$, the largest real part of eigenvalue crosses imaginary axis.

Computations were performed with a fluid filling fraction of 0.1, a fluid viscosity of 500*cSt*, a cylinder radius of 1.75 cm, and a rotation speed of 1–100 rpm, which correspond to the experimental conditions. When β is 5.72 (rotation speed is 1 rpm and $Re = 0.06$), the largest real part of the eigenvalue is negative as the wave number varies from 0 to 10 as depicted in Figure 5(a). (In the figure, only the cases of wave number below 6 were plotted.) It is observed that the largest real part is reduced as the wave number increases. As rotation speed increases ($\beta = 3.90$, Figure 5(b)), the largest real part does not demonstrate much difference as the wave number increases. We observed that the largest real parts of eigenvalues at wave numbers of 1 and 2 cross the imaginary axis when rotation speed is 15 rpm ($\beta = 1.47$ and $Re = 0.96$, Figure 5(c)). The β value for this critical rotation speed falls in the range of onset value of the transition between homogeneous film and bump states as described in the previous section. As β is decreased to less than the critical value as shown in Figure 5(d) ($\beta = 1.06$ and $Re = 1.86$), the eigenspectra with wave numbers 1, 2 and 3 demonstrate Hopf mode behaviour, where each wave speed is the corresponding imaginary part of the leading eigenvalues. In this case, the film thickness of axially wavy front is unstable and oscillates temporally. Additional computations with wave number less than 1 demonstrated

DOI: 10.1002/fld

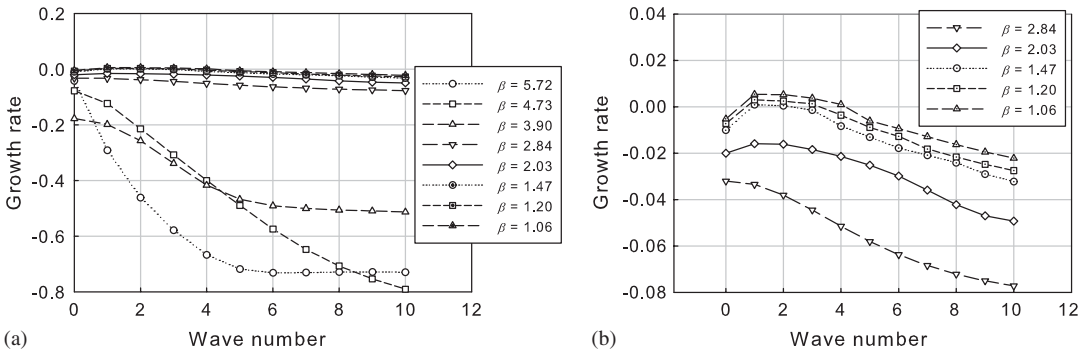

Figure 6. (a) Variation of largest real part of eigenvalue according to wave number at various β; and (b) magnified view: positive largest real part of eigenvalue.

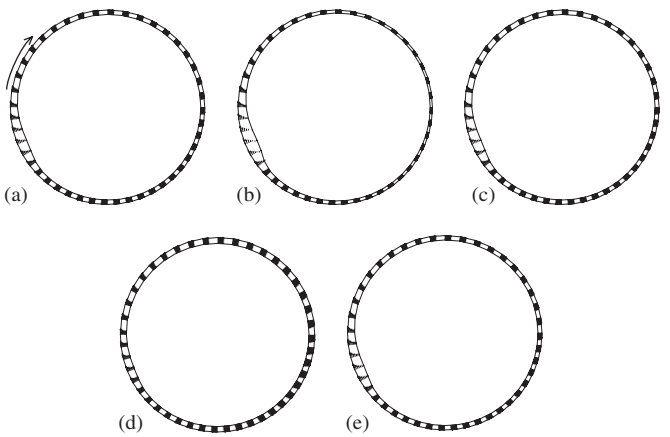

Figure 7. Reconstructed flow fields and free surface shape along the axial direction at $m=1$, $\beta=1.47$: (a) $z=0$; (b) $z=\pi/2$; (c) $z=\pi$; (d) $z=3\pi/2$; and (e) $z=2\pi$.

that the axial wavelength is almost twice longer than that for the non-Hopf mode case (i.e. when $m=0.5$). This phenomenon is observed experimentally by Melo [5]. As β decreases further, the largest real parts of eigenvalues decrease and as β becomes less than 0.8, all eigenvalues were observed to be negative, which means an axially stable flow.

Figure 6 shows the variation of the growth rate (largest real part of leading eigenvalue) according to β and wave number. When β is larger than 2.84, the growth rate is negative and decreases as wave number increases (Figure 6(a)). With the decrease of β, growth rate increases and crosses the abscissa of zero growth rate when β is less than 1.47. This is clearly depicted in the magnified view (Figure 6(b)). The critical condition appears to be in the vicinity of $\beta=1.47$ and $m=1$.

Figure 7 depicts the reconstructed flow field and interfacial height along the axial direction at critical wave number and β. We observed that the steady state velocity field described in the previous section is perturbed so that the bumpy shape and the recirculating flow in the bump are

DOI: 10.1002/fld

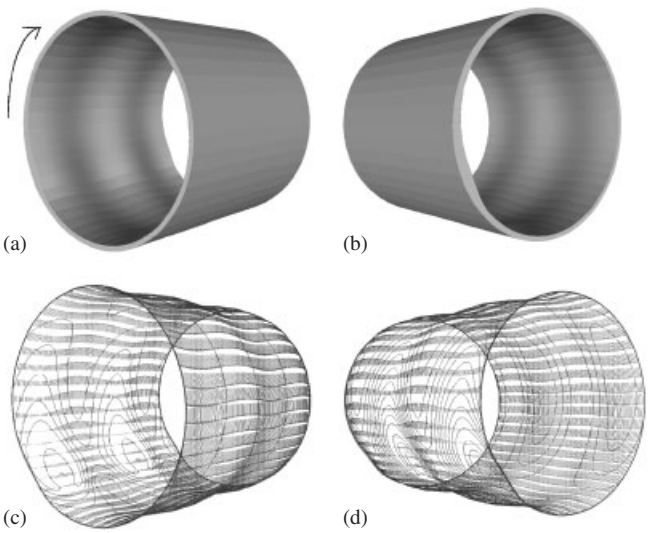

Figure 8. Three-dimensional view of the rising and falling sides of the cylinder surface at $m = 1$ and $\beta = 1.47$; free surface shape on: (a) the rising side; and (b) the falling side, the reconstructed velocity field on: (c) the rising side; and (d) the falling side. The axial range is from 0 to 4π in which the periodic oscillation of the perturbation appears twice.

formed when $z = \pi/2$ (Figure 7(b)). Except for the bumpy region, the flow pattern does not show much difference from the steady state. The only difference is the variation of film thickness in the z-direction.

Using the post-processing program, *Ensight*® 7.4, a three-dimensional view of the rising and falling sides of the cylinder surface at the critical conditions was obtained as depicted in Figure 8. The axially wavy feature of the free surface is clearly shown in Figures 8(a) and (b). Figures 8(c) and (d) depict the reconstructed velocity field on the fluid surface. The lines in the figures indicate the iso-contours of the velocity magnitude. Around the bumpy region, the velocity magnitude is observed to be at its minimum, which reveals the recirculating flow inside the bumpy region (inside the circular iso-contour lines). The reverse flow to the cylinder rotation is clearly observable on the bumpy region while the flow outside the bumpy region is in the same direction as the cylinder rotation.

Figure 9 shows a comparison of computational results to experimental results conducted under the same conditions. The onset condition of the instability acquired by computation is confirmed to be in agreement with experimental results. The computational result is plotted in the θ–z dimension, which depicts the velocity fields on the fluid surface. The range of θ is between -1.0 and 0.2 where the bump and the wavy front appear. The actual wavelength of the wavy front appears to be slightly smaller than the cylinder radius (the dimensional characteristic length), so that the measured dimensionless wave number is 0.96, which is comparable to the computational one. The recirculating flow with an opposite directional arrow is depicted in the figure.

The r–z cross-sectional views of r-, θ-, z-directional velocity contours and velocity field at $\theta = -0.5$ radian are depicted in Figure 10. Figure 10(a) demonstrates that, on the surface, the flow is radially outward at the ridge region and inward at the trough region. (The magnitude of normal

DOI: 10.1002/fld

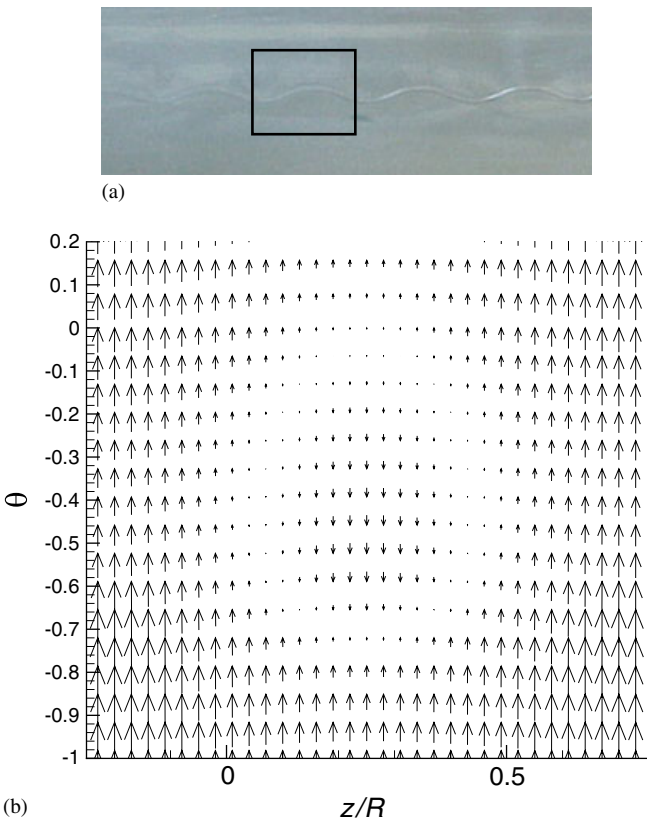

Figure 9. θ–z directional interface view: (a) of experiments; and (b) computational result (velocity field of the dot-box in (a)) at $m = 1$, $\beta = 1.47$, $\Omega = 15$ rpm, $F = 0.1$ and $v = 500cSt$.

velocity on the surface is not zero in this r–z cross-sectional plot.) The magnitude of radial velocity, except in the surface region, is almost zero. The recirculating motion is clearly observable in Figure 10(b). The azimuthal velocity is positive near the outer cylinder surface because of the no-slip condition, and negative at the surface of ridge because of recirculation. Figure 10(c) depicts how the fluid underneath the ridge axially separates to both sides of the ridge (in the trough regions), and fluid is drawn up along the trough region in an azimuthal direction. This depicted motion was also observed experimentally and computationally in the θ–z dimensional velocity plot as in Figure 9. Figure 10(d) depicts the r–z dimensional velocity plot. We observed U-shape clockwise or counter-clockwise flows at both sides of the bump.

The thickness of the coating film along the axial direction was measured experimentally and compared to the computational results as depicted in Figure 11. The thickness was measured by a needle attached to the end of a rod that was introduced into the cylinder through the hole on the end cap. The rod, in turn, was attached to a series of radial and angular traverses which allowed us to move the needle with a precision of 10^{-3} mm in the radial direction and 5° in the angular direction. In addition, the measuring system was mounted on an axial traverse such that the film thickness could also be measured at different axial positions along the length of the cylinder.

DOI: 10.1002/fld

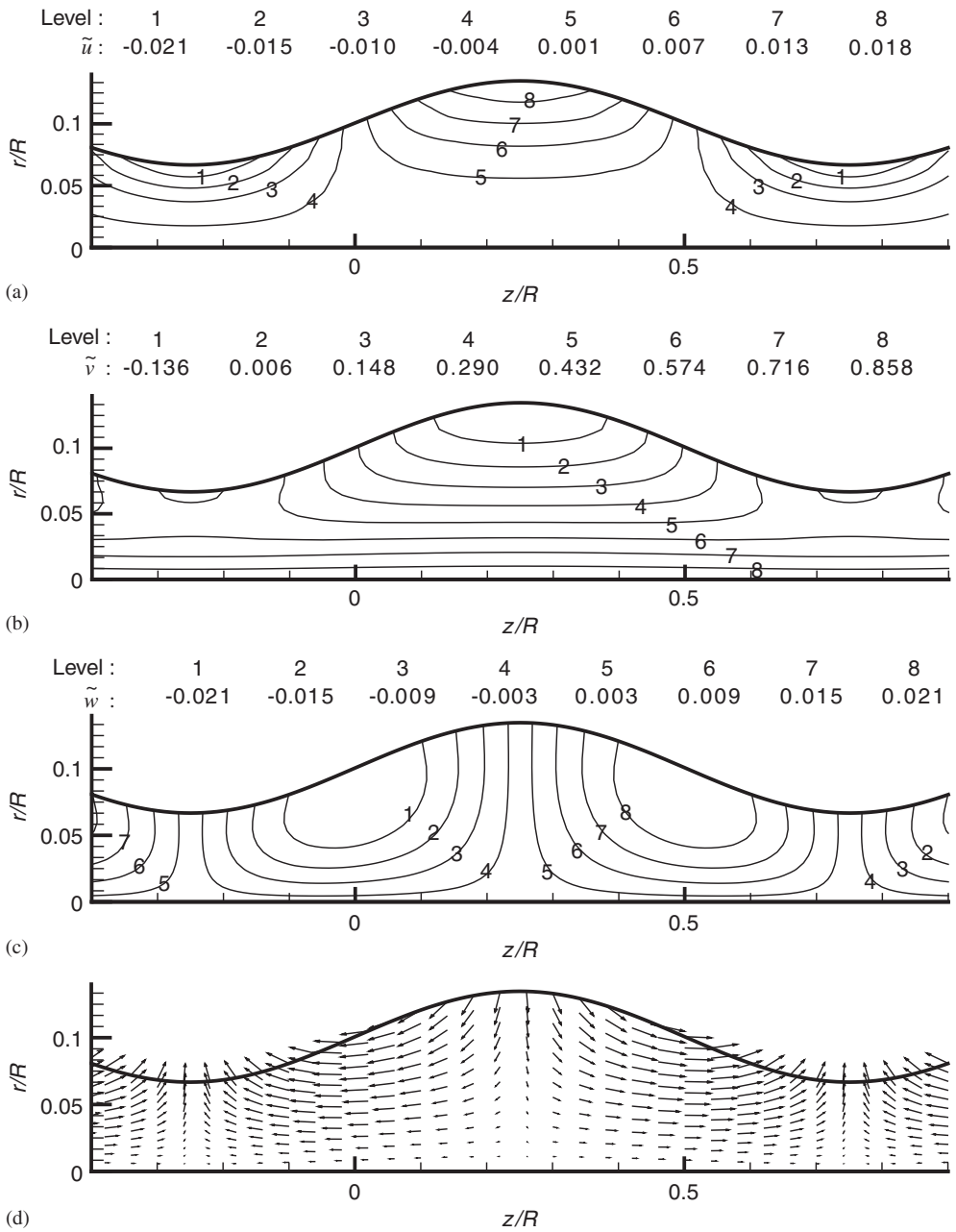

Figure 10. r–z cross-sectional view at $m=1$, $\beta=1.47$ and $\theta=-0.5$ radian: (a) r-directional; (b) θ-directional; (c) z-directional velocity contours; and (d) velocity field plot. The abscissa and ordinate values are normalized by the radius.

DOI: 10.1002/fld

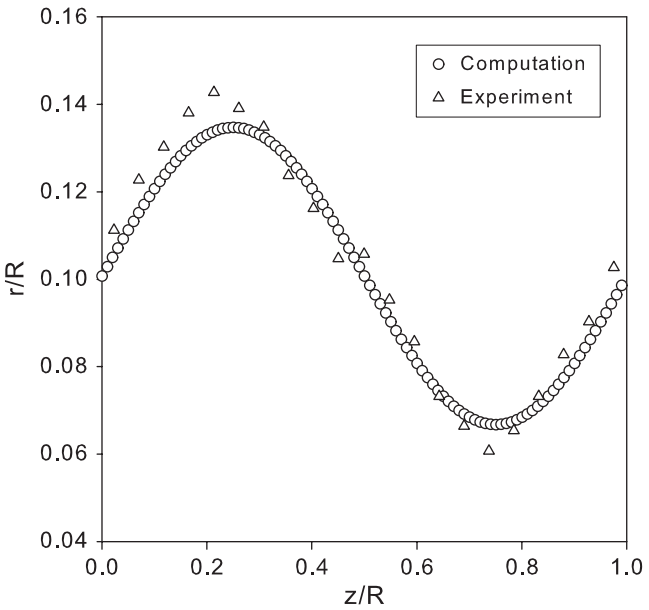

Figure 11. Comparison of interfacial height; computation results to experimental results at $m = 1$ and $\beta = 1.47$. The abscissa and ordinate values are normalized by the radius.

As shown in Figure 11, the computational data was in relatively good agreement with the experimental data. Experimental conditions are the same as in Figure 9(a).

In order to investigate the effects of surface tension on wavelength, we used a mixture of glycerin and water and modified the surface tension by the addition of sodium dodecyl sulphate (SDS). The surface tension of the liquid is 65 dyn/cm without addition and reduces to 52.5 dyn/cm after 0.5% addition. Experimental results were compared to computational results as depicted in Figure 12. We observed the same proportionality between wavelength and surface tension as mentioned in Huppert's work, who found that fingering instability of highly viscous fluid flowing down on an incline has a relation between wavelength and surface tension which is set up like [41],

$$\lambda = 7.5 \left(\frac{A^{1/2} \gamma}{\rho g \sin \alpha} \right)^{1/3} \tag{24}$$

Inertia effect is neglected in most previous analytic studies based on lubrication approximation, in which the axial instability was not observed. In the same manner we observed that axial instability does not occur when Reynolds number is much smaller than $O(1)$. In addition, eigenvalue problem of stability analysis derived from the Stokes' equation (neglecting inertia effect) does not result unstable state, which means that inertia effect is important on the generation of axial instability. Figure 13 is a phase diagram in Re–β space showing the regions of axial instability at a fluid filling fraction of 0.1 and surface tension of 21 dyn/cm, which shows that rimming flow is axially stable when Re is small. The parameters Re and β are chosen as they are only two independent combinations of the physical parameters, Ω, v, R, and g.

DOI: 10.1002/fld

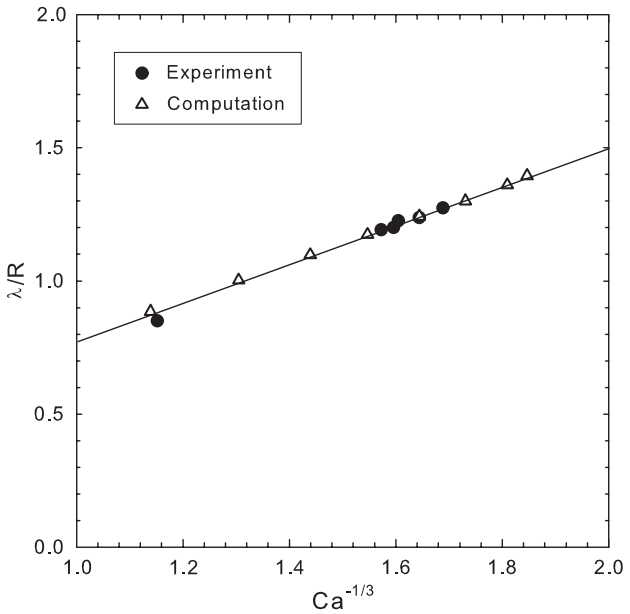

Figure 12. Variation of wavelength according to surface tension; comparison of computational and experimental results.

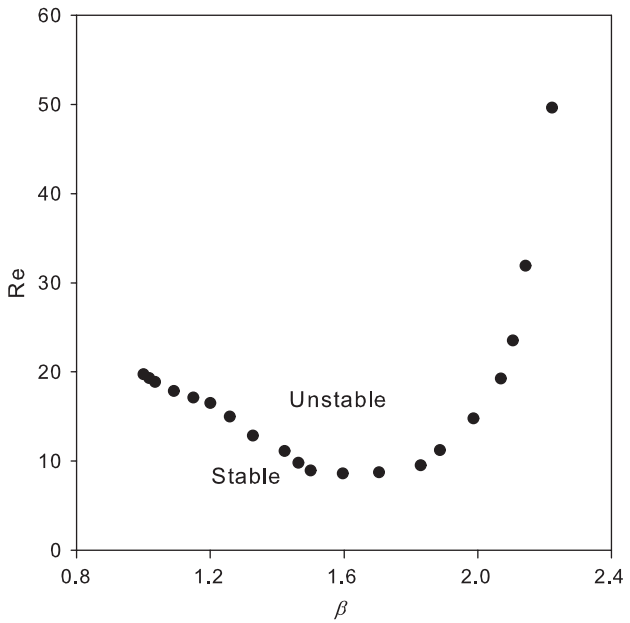

Figure 13. Numerically calculated phase diagram in Re–β space at fixed fluid filling fraction and surface tension showing the regions of stability and instability.

DOI: 10.1002/fld

5. CONCLUSIONS

By using the implicitly restarted Arnoldi method with shift-invert technique, we have observed the dominant parts of eigenvalues with a high degree of accuracy. The estimated critical results in this case, corresponding to our experiments, are 1.47 for β and unity for the critical wave number. These results are almost identical to the experimental observations. Three dimensionality in rimming flow is demonstrated through reconstruction of flows in the critical mode and it was confirmed that the wavelength of the wavy front is proportional to $-\frac{1}{3}$ power of the Capillary number. In addition, axial instability does not occur in the absence of inertia effect. This study provides the initial step for instability analysis of particle segregation in rimming flow by combining the particle conservation equation with the Navier–Stokes equations and the continuity equation.

ACKNOWLEDGEMENTS

The authors wish to acknowledge the support of the BK 21 project and the partial funding of this research by the Center for Ultramicrochemical Process Systems sponsored by KOSEF.

REFERENCES

1. Moffatt HK. Behavior of a viscous film on the outer surface of a rotating cylinder. *Journal of Mechanisms* 1977; **16**:651–673.
2. Balmer RT. The hydrocystal stability phenomenon in continuum mechanics. *Nature* 1970; **227**:600–601.
3. Hosoi AE, Mahadevan L. Axial instability of a free-surface front in a partially filled horizontal rotating cylinder. *Physics of Fluids* 1999; **11**:97–106.
4. Karweit MJ, Corrsin S. Observation of cellular patterns in a partly filled, horizontal, rotating cylinder. *Physics of Fluids* 1975; **18**:111–112.
5. Melo F. Localized states in a film-dragging experiment. *Physical Review E* 1993; **48**:2704–2712.
6. Thoroddsen S, Mahadevan L. Experimental study of coating flows in partially-filled horizontal rotating cylinder. *Experiments in Fluids* 1997; **23**:1–13.
7. Sanders J, Joseph DD, Beavers GS. Rimming flow of a viscoelastic liquid inside a rotating horizontal cylinder. *Journal of Non-Newtonian Fluid Mechanics* 1981; **9**:269–300.
8. Johnson RE. Steady-state coating flows inside a rotating horizontal cylinder. *Journal of Fluid Mechanics* 1988; **190**:321–342.
9. O'Brien SBG, Gath EG. The location of a shock in rimming flow. *Physics of Fluids* 1998; **10**:1040–1042.
10. Ruschak KJ, Scriven LE. Rimming flow of a liquid in a rotating horizontal cylinder. *Journal of Fluid Mechanics* 1976; **76**:113–125.
11. Duffy BR, Wilson SK. Thin film and curtain flows on the outside of a horizontal rotating cylinder. *Journal of Fluid Mechanics* 1999; **394**:29–49.
12. Hansen EB, Kelmanson MA. Steady, viscous, free-surface flow on a rotating cylinder. *Journal of Fluid Mechanics* 1994; **272**:91–107.
13. Kelmanson MA. Theoretical and experimental analyses of the maximum-supportable fluid load on a rotating cylinder. *Journal of Engineering Mathematics* 1995; **29**:271–285.
14. Peterson RC, Jimack PK, Kelmanson MA. On the stability of viscous free-surface flow supported by a rotating cylinder. *Proceedings of the Royal Society of London, Series A* 2001; **457**:1427–1445.
15. Preziosi L, Joseph DD. The run-off condition for coating and rimming flows. *Journal of Fluid Mechanics* 1988; **187**:99–113.
16. Pukhnachev VV. Motion of a liquid film on the surface of a rotating cylinder in a gravitational field. *Journal of Applied Mechanics and Technical Physics* 1977; **18**:344–351.
17. Wilson SK, Hunt R, Duffy BR. A new type of instability: explosive disturbances in a liquid film inside a rotating horizontal cylinder. *Quarterly Journal of Mechanics in Applied Mathematics* 2002; **55**:357–383.
18. Fomin S, Watterson J, Raghunathan S. The run-off condition for rimming flow of a power-law fluid. *Theoretical and Computational Fluid Dynamics* 2001; **15**:83–94.

DOI: 10.1002/fld

19. Wilson SDR, Williams J. The flow of a liquid film on the inside of a rotating cylinder, and some related problems. *Physics of Fluids* 1997; **9**:2184–2190.
20. Benjamin TB, Pritchard WG, Tavener SJ. Steady and unsteady flows of a highly viscous liquid inside a rotating horizontal cylinder. 1995, preprint.
21. Tirumkudulu M, Acrivos A. Coating flows within a rotating horizontal cylinder: lubrication analysis, numerical computations, and experimental measurements. *Physics of Fluids* 2001; **13**:14–19.
22. Orr FM, Scriven LE. Rimming flow: numerical simulation of steady, viscous, free-surface flow with surface tension. *Journal of Fluid Mechanics* 1978; **84**:145–165.
23. Peterson RC, Jimack PK, Kelmanson MA. On the stability of viscous free-surface flow supported by a rotating cylinder. *Proceedings of the Royal Society of London*, *Series A* 2001; **457**:1427–1445.
24. Hinch EJ, Kelmanson MA. On the decay and drift of free-surface perturbations in viscous thin-film flow exterior to a rotating cylinder. *Proceedings of the Royal Society of London*, *Series A* 2003; **459**:1193–1213.
25. Benilov ES, O'Brien SBG, Sazonov IA. A new type of instability: explosive disturbances in a liquid film inside a rotating horizontal cylinder. *Journal of Fluid Mechanics* 2003; **497**:201–224.
26. Ashmore JJ, Hosoi AE, Stone HA. The effect of surface tension on rimming flows in a partially filled cylinder. *Journal of Fluid Mechanics* 2003; **479**:65–98.
27. Govindarajan R, Nott PR, Ramaswamy S. Theory of suspension segregation in partially filled horizontal rotating cylinders. *Physics of Fluids* 2001; **13**(12):3517–3520.
28. Govindarajan R, Nott PR, Ramaswamy S. Stripes in sheared non-Brownian suspensions with a free surface. *Physica A* 2003; **318**:80–84.
29. Ramaman N, Homsy GM. Linear stability of lid-driven cavity flow. *Physics of Fluids* 1994; **6**:2690–2701.
30. Malkus DS. Eigenproblems associated with the discrete LBB condition for incompressible finite elements. *International Journal of Engineering Science* 1981; **19**:1299–1310.
31. Kessler R. Non-linear transition in three dimensional convection. *Journal of Fluid Mechanics* 1987; **174**:357–379.
32. Sackinger PA, Brown RA, Derby JJ. A finite element method for analysis of fluid flow. *International Journal for Numerical Methods in Fluids* 1989; **9**:453–492.
33. Hood P. Frontal solution program for unsymmetric matrices. *International Journal for Numerical Methods in Engineering* 1976; **10**:379–399.
34. Ding Y, Kawahara M. Linear stability of incompressible fluid flow in a cavity using finite element method. *International Journal for Numerical Methods in Fluids* 1998; **27**:139–157.
35. Saito H, Scriven LE. Study of coating flow by the finite element method. *Journal of Computational Physics* 1981; **42**:53–76.
36. Natarajan R. An Arnoldi-based iterative scheme for nonsymmetric matrix pencils arising in finite-element stability problems. *Journal of Computational Physics* 1992; **100**(1):128–142.
37. Saad Y. Variations on Arnoldi's method for computing eigenelements of large unsymmetric matrices. *Journal of Computational Physics* 1993; **108**:8–14.
38. Nour-Omid B, Dunbar WS, Woodbury AD. Lanczos and Arnoldi methods for the solution of convection–diffusion equations. *Computer Methods in Applied Mechanics and Engineering* 1991; **88**:75–95.
39. Meerbergen K. A theoretical comparison between inner products in the shift-invert Arnoldi method and the spectral transformation Lanczos method. *Electronic Transactions and Numerical Analysis* 1998; **7**:90–103.
40. Lehoucq RB, Lehoucq R, Sorensen DC, Yang C. *Arpack User's Guide*: *Solution of Large-Scale Eigenvalue Problems With Implicitly Restarted Arnoldi Methods*, Society for Industrial and Applied Mathematics: Philadelphia, 1998.
41. Huppert HE. Flow and instability of a viscous current down a slope. *Nature* 1982; **300**(2):427–429.

DOI: 10.1002/fld